Edge phonons in layered orthorhombic GeS and GeSe monochalcogenides

H. B. Ribeiro,[1] S. L. L. M. Ramos,[2] L. Seixas,[1] C. J. S. de Matos,[1,*] and M. A. Pimenta[3,†]

[1]*MackGraphe - Graphene and Nanomaterials Research Center, Mackenzie Presbyterian University, 01302-907 São Paulo, Brazil*

[2]*Centro de Tecnologia em Nanomateriais e Grafeno (CTNano), Universidade Federal de Minas Gerais, 30161-970 Belo Horizonte, Brazil*

[3]*Departamento de Física, UFMG, 30123-970 Belo Horizonte, Brazil*

(Received 15 November 2017; revised manuscript received 20 May 2019; published 3 September 2019)

Germanium sulfide (GeS) and germanium selenide (GeSe) are layered orthorhombic crystals whose structure bears a strong resemblance with that of black phosphorus and, additionally, are expected to exhibit high piezoelectricity in the few layer domain. In this work, we investigate the Raman properties of exfoliated GeS and GeSe and show that their edges exhibit unusual polarized Raman features that were first observed in black phosphorus. The results include the activation in the spectra of otherwise not allowed modes at the edges of the sample, depending on the crystallographic direction of the edge and the polarization configuration used in the measurements. These features are attributed to atomic rearrangements at the crystal terminations, as well as their impact on phonon symmetries, similar to the case of black phosphorus. Our conclusions are further corroborated by using density functional theory and suggest that edge rearrangements, which will have an impact on the mechanical, electronic, and chemical properties of devices, is a general phenomenon of orthorhombic layered structures.

DOI: 10.1103/PhysRevB.100.094301

I. INTRODUCTION

The exfoliation of graphite down to the monolayer thickness [1] has led to a drastic increase in the interest in the properties of layered materials, such as the hexagonal boron nitride (h-BN), transition metal dichalcogenides (TMD), and black phosphorus (BP) [2]. Particularly, BP is a semiconducting layered allotrope of phosphorus with a puckered orthorhombic structure and has drawn attention due to its interesting anisotropic physical properties [3–5] and its direct band gap that is readily tuned with the number of layers [6–8]. The group-IV monochalcogenide semiconductors GeS, GeSe, SnS, and SnSe [9] share the same layered puckered orthorhombic structure as BP. They also belong to point group D_{2h}, but with eight atoms per unit cell instead of four (space group *Pnma*, no. 62). In particular, GeS has a direct band gap of $\sim$1.65 eV [10–12] and GeSe has an indirect band gap of $\sim$1.14 eV [11,13].

Very recently, GeSe crystals were thinned down to a monolayer through the use of a laser and a transition from indirect to direct band gap identified for thicknesses of less than three layers [14]. While this result will contribute to future technological applications of monochalcogenides, the production of large pristine few-layer crystals is still a challenge. Moreover, while the anisotropic behavior of bulk crystals is well reported [15,16] and the impact of dimensionality reduction on the electronic structure has been theoretically predicted [9], detailed experimental characterization is still lacking. Unlike BP crystals, both GeS and GeSe crystals are stable when left in air, which makes them promising materials for the fabrication of a wide variety of devices, such as solar cells [17], tunnel field effect transistors for ultralow energy switching applications [18], photocatalysts for water splitting [19], and piezoelectric devices [20–22].

Along with the properties that arise due to the reduction of the dimensionality, the edges of layered materials have proved to be an interesting object of study due to their distinct magnetic, electronic, and optical properties [23–27], with important consequences for applications in optical and electronic devices. It has been recently reported that BP edges present an anomalous phonon behavior [28]. Using polarized Raman spectroscopy, modes that in bulk are symmetry forbidden at certain polarization configurations are observed at zigzag and/or armchair edges. The presence of such features was attributed to atom rearrangements at the crystal edges, which affect the atom displacements associated with vibrations.

In this paper, we report on a polarized Raman spectroscopy study performed at the edges of exfoliated GeS and GeSe crystals. The results show the same type of symmetry break in the selection rules of Raman active modes observed in BP. Considering the fact that group-IV monochalcogenides and BP share the same crystal structure, the features observed here are also assigned to atomic rearrangements at the edges. Our experimental results are further corroborated by density functional theory (DFT) calculations showing that atomic rearrangements indeed take place at the crystal's edges.

II. METHODS

GeS and GeSe crystals were obtained from HQ graphene with purity of >99.995%. The bulk crystals were exfoliated by using the common micromechanical exfoliation method, using an adhesive tape, and then transferred onto a silicon substrate with a 100-nm-thick silicon nitride layer (Si/Si_3N_4).

*cjsdematos@mackenzie.br

†mpimenta@fisica.ufmg.br

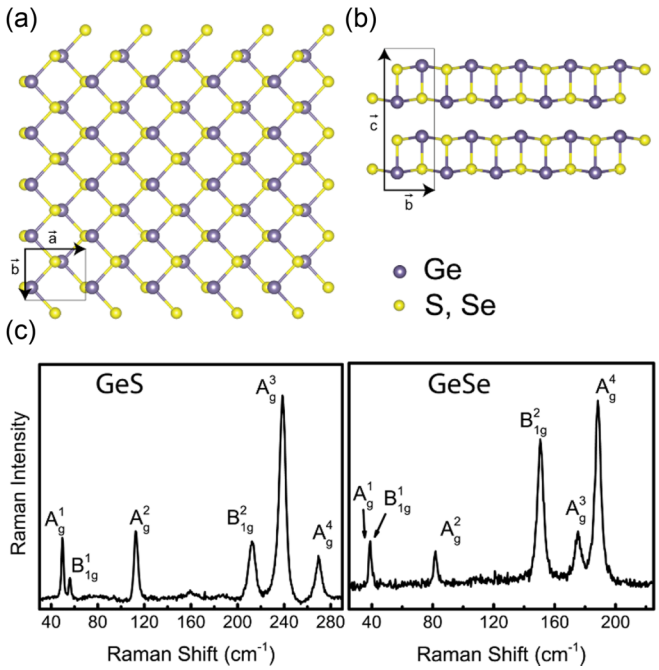

FIG. 1. GeS and GeSe crystal structure from (a) top and (b) lateral views. (c) Typical unpolarized Raman spectra of GeS and GeSe, with the mode symmetries indicated.

This choice of substrate was found to maximize the number of transferred flakes relative to the traditional silicon oxide on silicon (Si/SiO_2) substrate. This property can be partially attributed to the difference in the hydrophobic/hydrophilic character of these two substrates.

Raman measurements were initially performed using a WITec Alpha 300R confocal Raman microscope coupled with a RayShield coupler and a grating of 1800 g/mm, which allowed for inspection over the whole spectral range of interest, from <10 to 300 cm^{-1}. For polarized Raman spectroscopy, the Rayshield coupler was not used, thus limiting inspection of the polarized spectra to the 75 to 300 cm^{-1} range. In this case, an analyzer was placed before the spectrometer and edge features were compared with those from bulk by raster scanning the excitation laser beam along lines perpendicular to the edges while acquiring spectra (line scans). Two-dimensional hyperspectral Raman images were also acquired near flake edges. In both cases, the typical step size was 150 nm. All Raman measurements were performed using a 633 nm laser line.

For polarized Raman measurements, the incident light (linear) polarization remained fixed and the analyzer was adjusted to be either parallel or orthogonal to the incident polarization. The flakes under study exhibited a rectangular geometry [29], and their edges were aligned either parallel or orthogonal to the incident polarization. In addition, as will be shown, the edges were identified to be along specific crystallographic axes. Polarized Raman measurements were, therefore, performed in four different polarization configurations: c(a,a)$\bar{c}$, c(b,b)$\bar{c}$, c(a,b)$\bar{c}$, and c(b,a)$\bar{c}$, in which a, b, and c denote the three crystallographic axes (see Fig. 1). The first (last) index in the configuration names denotes the propagation direction of the incident (scattered) light, while the first (second) index between parentheses denotes the incident (analyzed) polarization. The overbar in the last index denotes characterization in the backscattering direction. It was found that GeS and GeSe flakes degraded under laser powers higher than 10 μW and 30 μW, respectively, when measurements took place in air with a 100× objective (0.9 numerical aperture). To avoid degradation, all measurements were performed under a constant nitrogen flow, which allowed the use of laser powers of 40 μW and 80 μW, respectively for GeS and GeSe, with no observed degradation.

TABLE I. Raman tensor forms for all Raman-active modes in GeS and GeSe.

Mode	A_g	B_{1g}	B_{2g}	B_{3g}
Tensor	$\begin{pmatrix} a & 0 & 0 \\ 0 & b & 0 \\ 0 & 0 & c \end{pmatrix}$	$\begin{pmatrix} 0 & d & 0 \\ d & 0 & 0 \\ 0 & 0 & 0 \end{pmatrix}$	$\begin{pmatrix} 0 & 0 & f \\ 0 & 0 & 0 \\ f & 0 & 0 \end{pmatrix}$	$\begin{pmatrix} 0 & 0 & 0 \\ 0 & 0 & g \\ 0 & g & 0 \end{pmatrix}$

For materials modeling and simulation, we used *ab initio* methods based upon DFT [30,31] as implemented in SIESTA code [32]. Our parameters for simulations are 300 Ry for energy cutoff, 0.03 eV for energy shift, DZP basis set, norm-conserved pseudopotentials with Troullier-Martins parametrization [33], and exchange-correlation functional with nonlocal correction of van der Waals interaction parametrized by Vydrov–van Voorhis [34]. k points in Brillouin zone were sampled with the Monkhorst-Pack method [35], with $15 \times 1 \times 6$ grid for zigzag edges and $1 \times 15 \times 6$ for armchair edges. All geometries were optimized with forces smaller than 0.010 eV/Å. Partial charges were calculated with Bader charge analysis [36].

III. RESULTS AND DISCUSSION

Figures 1(a) and 1(b) show the crystal structure for both GeS and GeSe in the top and lateral views, respectively. The lattice parameters were reported to be $a = 4.29$ Å, $b = 3.64$ Å, and $c = 10.42$ Å for GeS [37], and $a = 4.38$ Å, $b = 3.82$ Å, and $c = 10.79$ Å for GeSe [38], as obtained by x-ray diffraction. Notice that, while the lattice parameters are slightly different for the two crystals, the structure is the same and hence we use the same scheme to represent both crystals in Fig. 1. The unitary lattice vectors **a** and **b** are along the armchair and zigzag crystal directions, respectively, while **c** is perpendicular to the layer plane. The eight atoms per unit cell give rise to 24 vibrational modes, 12 of them being Raman active [39–41]. According to the character table for the D_{2h} point group and our choice of crystallographic axes, the expected Raman active mode symmetries are $4A_g$, $2B_{1g}$, $4B_{2g}$, and $2B_{3g}$ [39–41]. The Raman tensors [42] for all Raman active modes are given in Table I. Similar to the case of BP, all Raman tensor components exhibit, in principle, complex values [5]. Figure 1(c) shows typical unpolarized Raman spectra for GeS and GeSe flakes (away from edges).

According to the given Raman tensors, the only allowed modes when the propagation direction of the incident light is perpendicular to the *ab* plane are those with A_g and B_{1g} symmetries. From this property and previously reported measurements [39–41,43], the assignment of each peak is shown

TABLE II. Mode frequencies and symmetry assignments for all Raman-active modes. The middle column shows modes measured in this work; the right column shows mode frequencies extracted from the literature [40,44].

	Mode frequency (cm^{-1})											
Crystal	A_g^1	A_g^2	A_g^3	A_g^4	B_{1g}^1	B_{1g}^2	B_{2g}^1	B_{2g}^2	B_{2g}^3	B_{2g}^4	B_{3g}^1	B_{3g}^2
GeS	49	113	238	269	56	212	76	114	132	242	96	215
GeSe	39	81	175	188	39	150	72	105	203	231	42	159
GeS/GeSe frequency ratio	1.25	1.40	1.36	1.44	1.44	1.41	1.06	1.09	0.65	1.04	2.28	1.35

in Fig. 1(c). The symmetry assignments of the modes are given in Table II for both GeS and GeSe. For completeness, Table II also includes the modes that require incident polarization with components on the *ac* and *bc* planes. Since these modes are not visible in Fig. 1(c), frequencies were extracted from Refs. [40] and [44] for GeS and GeSe, respectively, and appear in the right column. The last row of Table II shows the ratio between the GeS and the GeSe frequencies for each mode. If a simple harmonic oscillator model for the Ge-Se or Ge-S vibrations is assumed, the resonance frequencies are expected to inversely scale with the square root of the reduced masses $\mu_{Ge-S,Se} = m_{Ge}m_{S,Se}/(m_{Ge} + m_{S,Se})$, where m_{Ge}, m_S, and m_{Se} are the masses of the germanium, sulfur, and selenium atoms, respectively. In this model, the frequency ratios would be $\sqrt{\mu_{Ge-Se}/\mu_{Ge-S}} = 1.30$, which approximately matches the ratios for many of the modes shown in Table II.

Next, we analyze the results obtained via polarized Raman spectroscopy. Figures 2(a) and 2(b) show optical microscope images of the measured GeS and GeSe flakes, which had 27 nm and 60 nm of thickness, respectively, as measured by atomic force microscopy. The bottom curves in Figs. 2(c)–2(f) show the polarized Raman spectra at the center of the GeS flake for all measured polarization configurations. Similar spectra for GeSe are shown in Fig. S1 in the Supplemental Material [45]. All spectra were normalized by their highest intensity peak. All peaks are labeled according to the assigned mode symmetries. Black labels indicate modes that are expected in each polarization configuration, blue labels indicate unexpected modes for that given polarization configuration, while red labels indicate modes that should not be present in any configuration in which the laser propagates along the **c** crystal direction. It can be seen that the spectra taken at the center of the flakes do not present unexpected peaks.

The GeS crystallographic orientation was found using the angular dependence of the polarized Raman spectra taken at the flake centers. As previously reported [40], while the A_g^2 mode is present in the c(a,a)$\bar{c}$ polarization configuration, it is completely absent from the c(b,b)$\bar{c}$ configuration. This can be observed in the bottom curves of Figs. 2(c) and 2(d), which show the polarized Raman spectra measured in the c(a,a)$\bar{c}$ and c(b,b)$\bar{c}$ configurations, respectively. The orientation for the GeSe flake was determined by comparing the relative intensities of the A_g^2 and A_g^3 modes with those in previous polarized Raman spectroscopy results [43,44]. Moreover, from the similarities between the crystals, it is reasonable to expect in GeSe that the *b* component of the A_g^2 tensor is smaller than the *a* component, as observed in case of GeS, leading to a smaller A_g^2 intensity in the c(b,b)$\bar{c}$ configuration than in the c(a,a)$\bar{c}$ configuration. This is indeed observed with our crystallographic axis assignment, as shown in the polarized Raman spectra GeSe available in Fig. S1 of the Supplemental Material [45].

Figures 2(c)–2(f) also show the spectra taken at the armchair and zigzag edges, as indicated in each curve, of the GeS flake, in the four analyzed polarization configurations. It is evident that all spectra taken at edges present unexpected

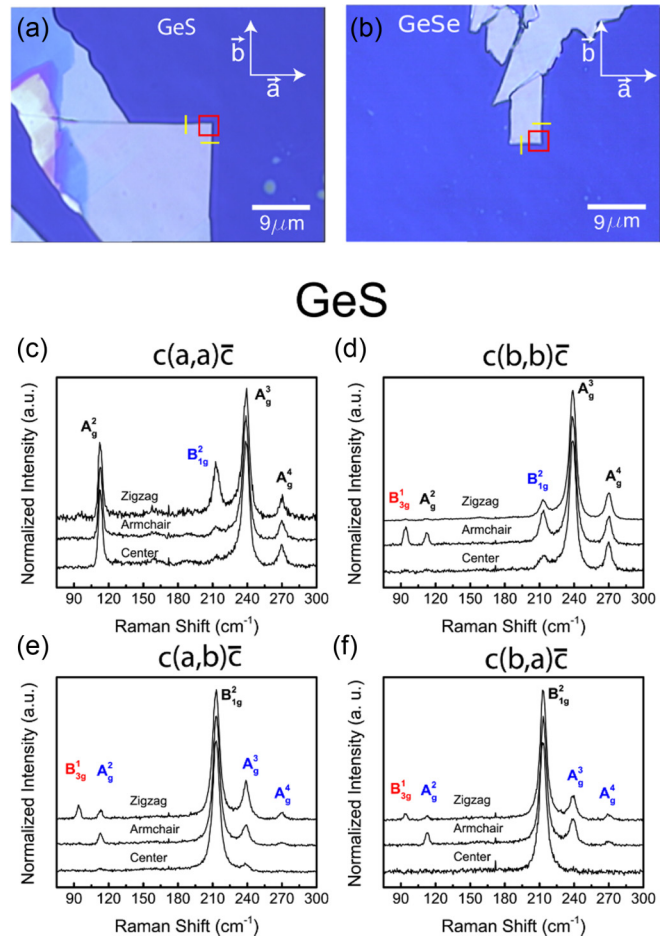

FIG. 2. Optical microscopy images of the measured (a) GeS and (b) GeSe flakes. The crystallographic axes are indicated in white. The red squares indicate the regions investigated via hyperspectral Raman imaging, while the yellow lines are the directions and regions where line scans were performed. (c)–(f) Polarized Raman spectra obtained with the indicated polarization configurations at the center (bottom) of the flake, and at the armchair (middle) and the zigzag (top) edges. The mode symmetries for each peak are indicated.

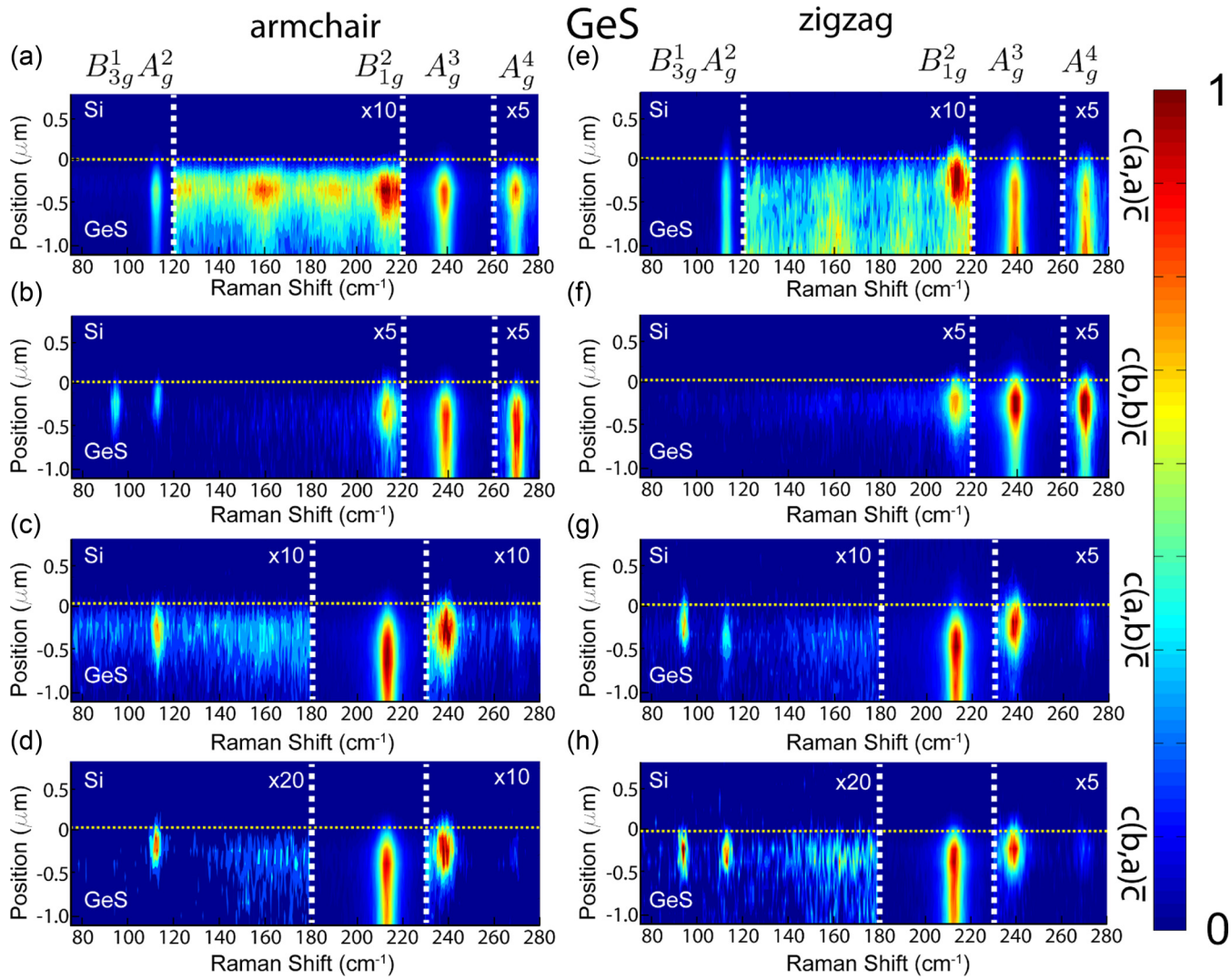

FIG. 3. Raman line scan images obtained with the GeS flake at the (a)–(d) armchair and (e)–(h) zigzag edges, using four different polarization configurations [from top to bottom c(a,a)c̄, c(b,b)c̄, c(a,b)c̄, and c(b,a)c̄ configurations, respectively]. Yellow dashed lines delimit the flake edges. The color scale represents the spectral intensities, which were normalized by the highest value in each image. White dashed lines delimit spectral regions in which the intensity was multiplied by a constant factor (indicated next to the dashed lines) for better visualization. The mode symmetries for each peak are indicated on top of the figure.

features. For example, as shown in Fig. 2(c), the B^2_{1g} mode, which should not be present in parallel polarization configurations, appears at the zigzag edge for the c(a,a)c̄ configuration. Figure 2(d) shows that this mode also appears at the armchair edge in the c(b,b)c̄ configuration. Moreover, several A_g modes appear in crossed polarization configurations as shown in Figs. 2(e) and 2(f). In addition, the B^1_{3g} mode, which should not appear under laser incidence along the **c** axis, is clearly present at the armchair and zigzag edges in the c(b,b)c̄ and c(a,b)c̄ configurations, as shown respectively in Figs. 2(d) and 2(e).

In order to better visualize the appearance of such unexpected features, Raman spectra were taken along lines perpendicular to each edge (line scans), in all polarization configurations. Figures 3(a)–3(h) show the line scans obtained in the GeS flake along the yellow lines indicated in Fig. 2(a), while Figs. 4(a)–4(h) show the line scans for the GeSe flake measured along the yellow lines of Fig. 2(b). Each image represents the spectrum, where the intensities are given in color scales, as a function of position. The images are arranged in columns, each one representing a different type of edge, and each row represents a different polarization configuration. In each image, the yellow dashed line marks the exact edge position. Regions delimited by white dashed lines are multiplied by the indicated constant factor, for better visualization.

From Figs. 3 and 4, we observe three sets of anomalous results. First, some allowed modes have their intensities increased at the edge. For example, both in GeS and GeSe, the A^2_g mode (at 113 cm^{-1} and 81 cm^{-1}, respectively) is enhanced at the armchair edge in the c(a,a)c̄ configuration [Figs. 3(a) and 4(a)]. Likewise, the B^2_{1g} mode in GeS (212 cm^{-1}) is enhanced at the armchair and zigzag edges in the c(a,b)c̄ and c(b,a)c̄ configurations [Figs. 3(c), 3(d) 3(g), and 3(h)]. The second type of feature is the appearance of modes that are not allowed in the measured polarization configuration, but

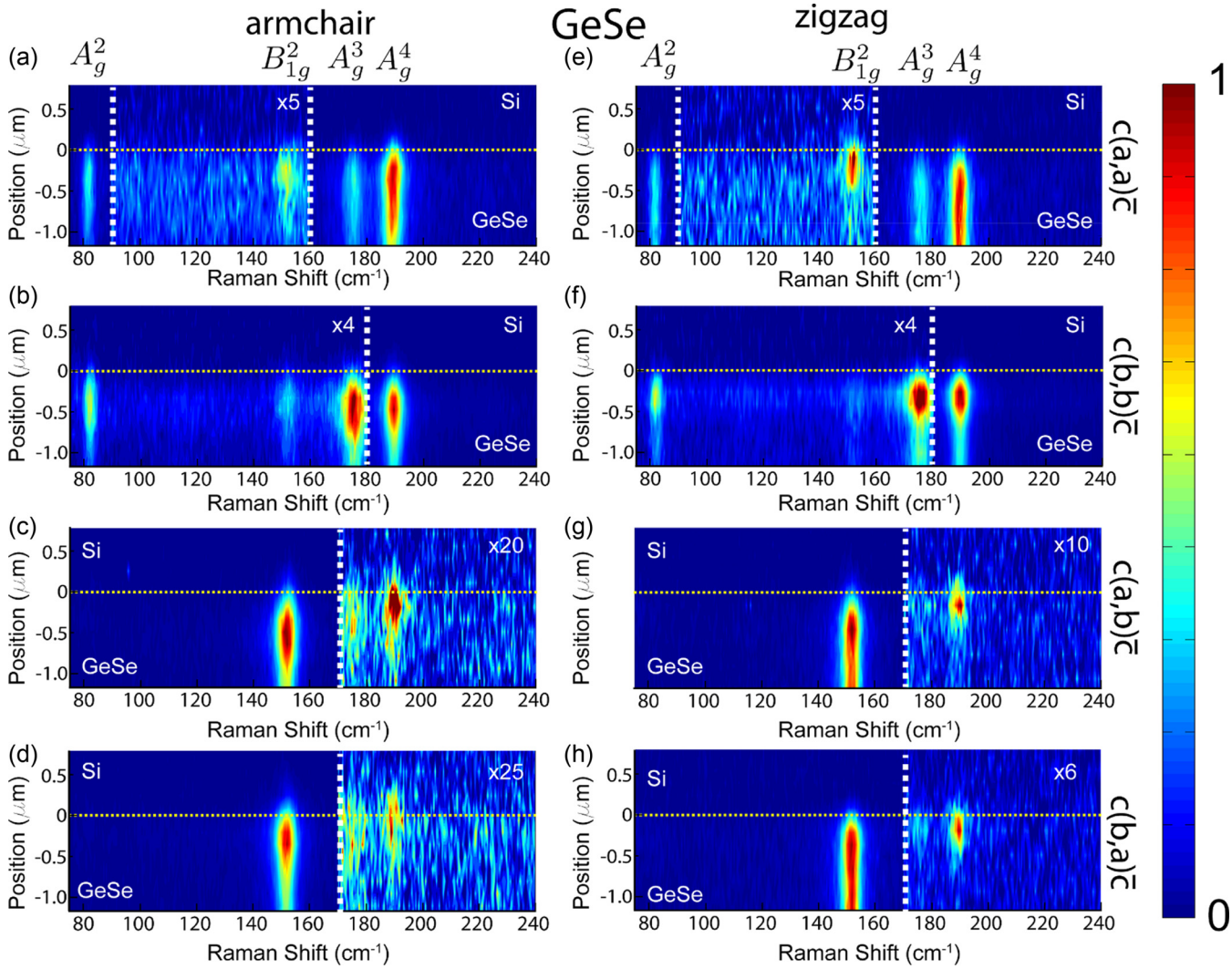

FIG. 4. Raman line scan images obtained with the GeSe flake at the (a)–(d) armchair and (e)–(h) zigzag edges, using the four different polarization configurations (from top to bottom c(a,a)c̄, c(b,b)c̄, c(a,b)c̄, and c(b,a)c̄ configurations, respectively). Yellow dashed lines delimit the flake edges. The color scale represents the spectral intensities, which were normalized by the highest value in each image. White dashed lines delimit spectral regions in which the intensity was multiplied by a factor (indicated next to the dashed lines) for better visualization. The mode symmetries for each peak are indicated on top of the figure.

which are expected in other configurations with incident light propagating along the **c** crystal direction. For example, the B_{1g}^2 mode in GeS and GeSe appears at the zigzag edge in the c(a,a)c̄ and c(b,b)c̄ configurations [Figs. 3(e) and 3(f) and 4(e) and 4(f)], and the A_g^2 mode in GeS arises at the armchair and zigzag edges in the c(a,b)c̄ and c(b,a)c̄ configurations [Figs. 3(c), 3(d) 3(g), and 3(h)].

The third anomalous result observed in our measurements is the appearance of modes that should only be present when the incident light does not propagate in the crystallographic direction **c**. This is observed for GeS in Fig. 3(b), in which the B_{3g}^1 mode (at 96 cm^{-1}) clearly appears at the armchair edge in the c(b,b)c̄ configuration, and in Figs. 3(g) and 3(h) that show the same mode appearing at the zigzag edge respectively in the c(a,b)c̄ and c(b,a)c̄ configurations. Note that this result was observed only for GeS, because in the case of GeSe, the B_{3g}^1 mode (at 42 cm^{-1}) is out of the range used for line scan measurements. In addition, even using the extended range setup for acquiring point spectra, this mode is almost degenerate with the A_g^1 mode (at 39 cm^{-1}) and spectral resolution limitation prevents its clear identification.

In order to verify if these features are present along the entire edge, hyperspectral Raman images were obtained in both the GeS and GeSe flakes in the regions indicated by the red squares in Figs. 2(a) and 2(b). Figures 5(a)–5(d) show the hyperspectral Raman images of the A_g^2, A_g^3, B_{1g}^2, and A_g^3 modes for the GeS flake in the c(a,a)c̄, c(b,b)c̄, c(b,b)c̄, and c(b,a)c̄ polarization configurations, respectively, while Figs. 5(e) and 5(f) show similar images for the A_g^4 mode of the GeSe flake in the c(a,a)c̄ and c(b,b)c̄ polarization configurations, respectively. The intensities in all images are presented in logarithm scale for better visualization. Additional hyperspectral Raman images, for other modes and polarization configurations, are provided in Fig. S2 of the Supplemental Material [45]. Indeed, in all cases we observe that the features are present along the whole edges.

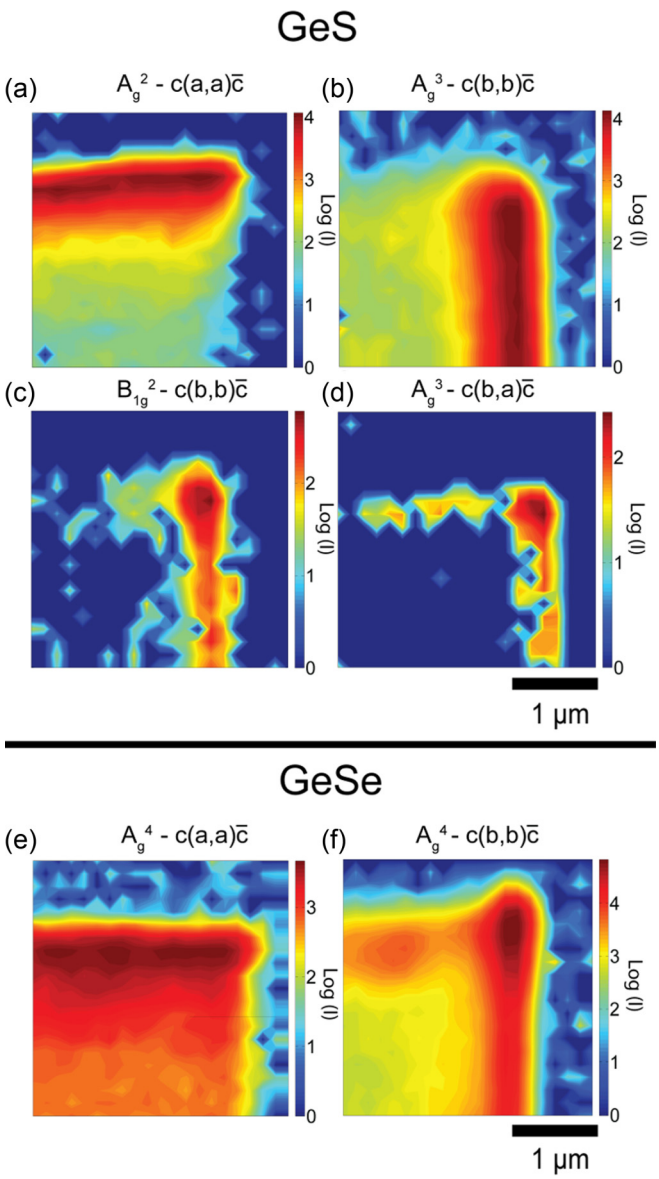

FIG. 5. Hyperspectral Raman images of selected modes and polarization configurations, taken within the red squares from Fig. 2 for the (a)–(d) GeS and (e)–(f) GeSe flakes. The intensities in all images are in logarithmic color scales.

A summary of all observed features is presented in Table III, in which triangles, squares, and diamonds respectively indicate the observation of the three types of anomalous results discussed above. The appearance of modes in configurations where they are not expected is connected to local changes in the crystal symmetry, leading to changes in the Raman tensors. For instance, A_g modes, for which the Raman tensors only possess diagonal components, are expected to be observed only in the parallel polarization configurations c(a,a)c̄ and c(b,b)c̄. However, three A_g modes are observed at the edges of GeS and two A_g modes of GeSe emerge in the c(a,b)c̄ and c(b,a)c̄ configurations, meaning that the corresponding Raman tensors acquire off-diagonal components. We stress that these anomalous results have been previously reported for BP [28,46] and density functional theory calculations showed that they arise as a consequence of edge reconstruction, with atomic rearrangements occurring near the crystal terminations.

Similar results were later observed at the center of BP flakes by Wang *et al.* [46], but with lower intensities compared with the intensity of the modes at edges. These features were attributed to the presence of a **c** component in the light polarization, which arises when the laser is focused by the microscope objective. Due to the low **c** component field amplitude, this effect was only observed when the laser energy was in resonance with electronic transitions. We stress that we did not observe any anomalous modes at the center of the flakes, since we are likely to be away from resonances. Moreover, considering the objective used in our experiments (a 100× Zeiss objective with numerical aperture of 0.9) and the laser wavelength (633 nm), we expect the depth of focus (DOF) to be around 500 nm (see the Supplemental Material [45]), which is much larger than the thicknesses of the investigated flakes. Under these conditions, the **c** field component is expected to be negligible and we conclude that the anomalous signal observed is related to crystal edges.

Recently, Guo *et al.* reported on similar Raman anomalies at the edges of MoS_2, WS_2, WSe_2, PtS_2, and BP [47], which were attributed to a drastic distortion of the electromagnetic field, of both the incident and scattered light, produced by the edges. Such distortions result in the appearance of new electric field components, which can also lead to the observation of forbidden modes. While a distorted electromagnetic field can explain some of our results, some contradictions arise. First, such a purely optical effect should give rise to the observation of the same modes in GeS and GeSe, as indeed observed for all transition metal dichalcogenides investigated by Guo *et al.* In contrast, a number of modes that are observed in GeS were not observed in GeSe, under the same conditions, as a quick look at Table II can confirm. For instance, the A_g^2 mode is observed at both edges in the c(a,b)c̄ and c(b,a)c̄ configurations for GeS, but is not observed in GeSe. Note that the GeSe crystal we probed is more than twice as thick as the GeS sample, which would make the electromagnetic distortion more apparent [47]. Furthermore, some selection rule contradictions arise when only the electromagnetic distortion picture is considered. For example, for GeS the absence of the A_g^2 mode in the c(b,b)c̄ configuration means that the b component of the Raman tensor shown in Table I is zero. Therefore, the increase in the A_g^2 mode in the armchair edge for the c(a,a)c̄ configuration [Fig. 3(a)] can only arise as a result of the appearance of a **c** component in the electric field. However, this component would also result in the observation of B_{2g} modes. In contrast, we did not observe B_{2g} modes in any configuration. These considerations indicate that edge reconstruction may play an important role to explain the appearance of forbidden modes, as in the case of BP.

To confirm this, the edge structures were calculated using *ab initio* modeling and simulations based on DFT (see Methods). To investigate the effect of structural relaxation, we created a periodic system in the direction perpendicular to the basal plane and in one of the directions parallel to these basal planes (zigzag or armchair). For simplicity, only the GeS material was studied in our *ab initio* simulations. We expect similar results for GeSe. For taking into account the ambient

TABLE III. Summary of features observed at the edges of GeS and GeSe flakes. Triangles indicate the enhancement of modes that were already expected in a given polarization configuration; squares denote the appearance of modes that are unexpected in that polarization configuration, but that are expected in other configurations with light propagating along the **c** crystal direction; diamonds indicate the appearance of modes that should not be present in any configuration with light propagating along the **c** direction. AC: armchair; ZZ: zigzag.

		GeS						GeSe			
Mode	Edge	c(a,a)$\bar{c}$	c(b,b)$\bar{c}$	c(a,b)$\bar{c}$	c(b,a)$\bar{c}$	Mode	Edge	c(a,a)$\bar{c}$	c(b,b)$\bar{c}$	c(a,b)$\bar{c}$	c(b,a)$\bar{c}$
A_g^2	AC	△	△	□	□	A_g^2	AC	△	△		
	ZZ			□	□		ZZ		△		
A_g^3	AC	△		□	□	A_g^3	AC	△	△		
	ZZ			□	□		ZZ		△		□
A_g^4	AC	△	△	□	□	A_g^4	AC	△	△	□	□
	ZZ		△	□	□		ZZ		△	□	□
B_{1g}^2	AC		□	△	△	B_{1g}^2	AC	□	□	△	△
	ZZ	□	□	△	△		ZZ	□	□		
B_{3g}^1	AC		◇			B_{3g}^1	AC				
	ZZ			◇	◇		ZZ				

conditions in which the GeS/GeSe flakes were measured, we optimized the geometries of flakes with zigzag and armchair edges, with and without dangling bond passivation.

Figure 6 shows ball-and-stick representations of the relaxed structures. For zigzag edges, seen in Figs. 6(b)–6(d) and 6(f)–6(h), there were significant changes in edge geometries depending on bond passivation. We investigated three zigzag edges, with different terminations: S terminations, Ge terminations, and alternating Ge-S terminations. When there is no bond passivation, a reconstruction at GeS edges is formed connecting the layers through covalent bonds as shown by the shaded gray area in Figs. 6(b)–6(d). This bond must occur due to the electrical polarity of the GeS: cations (Ge) interact with anions (S) from the adjacent layer. Partial charge analysis for Ge-terminated zigzag edges is shown in Fig. S4 of the Supplemental Material [45]. We observed that the interlayer interaction induces reconstructions observed in geometry optimization. When there is H passivation on dangling bonds, we observed no interlayer covalent bonds but significant bond elongations along the zigzag direction occur, as shown in Figs. 6(f)–6(h). For armchair edges, both without and with H passivation, Figs. 6(a) and 6(e) respectively show lower, yet noticeable, changes in edge geometry. These edge reconstructions are believed to cause the observed anomalies in the Raman spectra, as in the case of BP, and may impact on the thermal, mechanical, chemical, and electronic properties of nanodevices based on the investigated monochalcogenides.

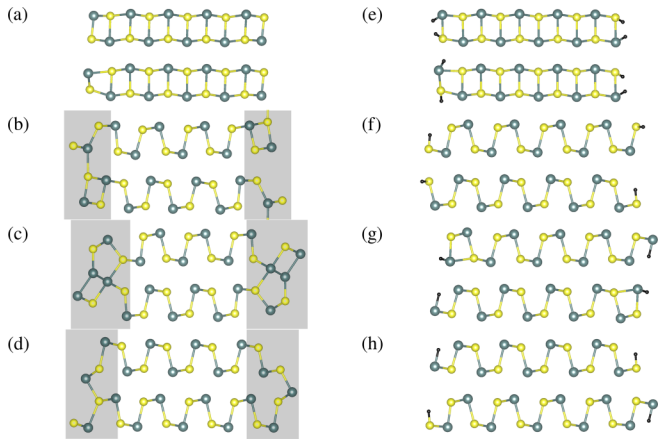

FIG. 6. Ball-and-stick representation of GeS edges. (a)–(d) GeS with unpassivated dangling bonds. (e)–(h) GeS with H-passivated dangling bonds. (a) Armchair edges; (b) S-terminated zigzag edges; (c) Ge-terminated zigzag edges; (d) alternating Ge-S zigzag edges; (e) H-passivated armchair edges; (f) SH-terminated zigzag edges; (g) GeH-terminated zigzag edges; (h) GeHSH-terminated zigzag edges. For (b)–(d), interlayer covalent bonds are shown in the shaded gray areas. Color scheme: Ge (green), S (yellow), and H (black).

IV. CONCLUSIONS

A polarized Raman spectroscopy study was carried out at the edges of exfoliated flakes of orthorhombic GeS and GeSe crystals, revealing the emergence of unexpected modes in the spectra. The flakes exhibit well-defined armchair and zigzag edges and four different polarization configurations were used to collect the spectra. The Raman spectra acquired at the center of the flakes exhibited the symmetry selection rules predicted by group theory and were used to identify the crystallographic axes. In contrast, the polarized Raman spectra at the edges revealed three sets of unexpected results: the enhancement of allowed modes at the edges, the appearance of modes that should only be present in other in-plane polarization configurations, and the appearance of modes that should not be present in a backscattering configuration with light propagating along the **c** direction. The appearance of such features was previously observed for black phosphorus (BP) crystals, which possess the same crystal structure as the monochalcogenides investigated here. The experimental results presented in this work can be explained as a consequence of atom rearrangements at the crystal's edges. This interpretation was supported by simulations based on DFT, which suggested that not only an atomic rearrangement takes place, but also that passivation impacts on the edge geometry. This behavior appears to be a general trend in layered crystals with the orthorhombic symmetry and will have an impact on the development of nanodevices based on these materials.

ACKNOWLEDGMENTS

This work is supported by FAPESP (SPEC Project No. 2012/50259-8 and Thematic Project No. 2015/11779-4), the Brazilian Nanocarbon Institute of Science and Technology (INCT/Nanocarbono), Fapemig, CNPq, CAPES PRINT (Programa Institucional de Internacionalização; Grant No. 88887.310281/2018-00), and MackPesquisa. H.B.R. acknowledges a CNPq scholarship and FAPESP fellowships (Grants No. 2017/20100-0 and No. 2018/04926-9). L.S. acknowledges the computational facilities from SDumont/LNCC supercomputer.

[1] K. S. Novoselov, A. K. Geim, S. V. Morozov, D. Jiang, Y. Zhang, S. V. Dubonos, I. V. Grigorieva, and A. A. Firsov, Science **306**, 666 (2004).

[2] S. Z. Butler, S. M. Hollen, L. Cao, Y. Cui, J. A. Gupta, H. R. Gutiérrez, T. F. Heinz, S. S. Hong, J. Huang, A. F. Ismach, E. Johnston-Halperin, M. Kuno, V. V. Plashnitsa, R. D. Robinson, R. S. Ruoff, S. Salahuddin, J. Shan, L. Shi, M. G. Spencer, M. Terrones, W. Windl, and J. E. Goldberger, ACS Nano **7**, 2898 (2013).

[3] S. P. Koenig, R. A. Doganov, H. Schmidt, A. Castro Neto, and B. Özyilmaz, Appl. Phys. Lett. **104**, 103106 (2014).

[4] J. Qiao, X. Kong, Z.-X. Hu, F. Yang, and W. Ji, Nat. Commun. **5**, 4475 (2014).

[5] H. B. Ribeiro, M. A. Pimenta, C. J. S. de Matos, R. L. Moreira, A. S. Rodin, J. D. Zapata, E. A. T. de Souza, and A. H. Castro Neto, ACS Nano **9**, 4270 (2015).

[6] A. Castellanos-Gomez, L. Vicarelli, E. Prada, J. O. Island, K. Narasimha-Acharya, S. I. Blanter, D. J. Groenendijk, M. Buscema, G. A. Steele, J. Alvarez *et al.*, 2D Mater. **1**, 025001 (2014).

[7] A. N. Rudenko and M. I. Katsnelson, Phys. Rev. B **89**, 201408(R) (2014).

[8] S. Zhang, J. Yang, R. Xu, F. Wang, W. Li, M. Ghufran, Y.-W. Zhang, Z. Yu, G. Zhang, Q. Qin, and Y. Lu, ACS Nano **8**, 9590 (2014).

[9] L. C. Gomes and A. Carvalho, Phys. Rev. B **92**, 085406 (2015).

[10] J. Wiley, A. Breitschwerdt, and E. Schönherr, Solid State Commun. **17**, 355 (1975).

[11] R. Eymard and A. Otto, Phys. Rev. B **16**, 1616 (1977).

[12] D. Tan, H. E. Lim, F. Wang, N. B. Mohamed, S. Mouri, W. Zhang, Y. Miyauchi, M. Ohfuchi, and K. Matsuda, Nano Res. **10**, 546 (2017).

[13] D. D. Vaughn II, R. J. Patel, M. A. Hickner, and R. E. Schaak, J. Am. Chem. Soc. **132**, 15170 (2010).

[14] H. Zhao, Y. Mao, X. Mao, X. Shi, C. Xu, C. Wang, S. Zhang, and D. Zhou, Adv. Funct. Mater. **28**, 1704855 (2018).

[15] C. Kannewurf and R. Cashman, J. Phys. Chem. Solids **22**, 293 (1961).

[16] M. Lisitsa, A. Zakharchuk, S. Terekhova, G. Tsebulya, S. Todorov *et al.*, Phys. Status Solidi B **75**, K51 (1976).

[17] Y. Mao, C. Xu, J. Yuan, and H. Zhao, Phys. Chem. Chem. Phys. **20**, 6929 (2018).

[18] M. Brahma, A. Kabiraj, D. Saha, and S. Mahapatra, Sci. Rep. **8**, 5993 (2018).

[19] C. Chowdhury, S. Karmakar, and A. Datta, J. Phys. Chem. C **121**, 7615 (2017).

[20] L. C. Gomes, A. Carvalho, and A. H. Castro Neto, Phys. Rev. B **92**, 214103 (2015).

[21] R. Fei, W. Li, J. Li, and L. Yang, Appl. Phys. Lett. **107**, 173104 (2015).

[22] T. Hu and J. Dong, Phys. Chem. Chem. Phys. **18**, 32514 (2016).

[23] A. H. Castro Neto, F. Guinea, and N. M. R. Peres, Phys. Rev. B **73**, 205408 (2006).

[24] X. Yin, Z. Ye, D. A. Chenet, Y. Ye, K. O'Brien, J. C. Hone, and X. Zhang, Science **344**, 488 (2014).

[25] Y.-W. Son, M. L. Cohen, and S. G. Louie, Nature (London) **444**, 347 (2006).

[26] Y. Li, Z. Zhou, S. Zhang, and Z. Chen, J. Am. Chem. Soc. **130**, 16739 (2008).

[27] E. V. Castro, N. M. R. Peres, J. M. B. Lopes dos Santos, A. H. Castro Neto, and F. Guinea, Phys. Rev. Lett. **100**, 026802 (2008).

[28] H. B. Ribeiro, C. E. P. Villegas, D. A. Bahamon, D. Muraca, A. H. Castro Neto, E. A. T. de Souza, A. R. Rocha, M. A. Pimenta, and C. J. S. de Matos, Nat. Commun. **7**, 12191 (2016).

[29] Y. Guo, C. Liu, Q. Yin, C. Wei, S. Lin, T. B. Hoffman, Y. Zhao, J. Edgar, Q. Chen, S. P. Lau *et al.*, ACS nano **10**, 8980 (2016).

[30] P. Hohenberg and W. Kohn, Phys. Rev. **136**, B864 (1964).

[31] W. Kohn and L. J. Sham, Phys. Rev. **140**, A1133 (1965).

[32] J. M. Soler, E. Artacho, J. D. Gale, A. García, J. Junquera, P. Ordejón, and D. Sánchez-Portal, J. Phys.: Condens. Matter **14**, 2745 (2002).

[33] N. Troullier and J. L. Martins, Phys. Rev. B **43**, 1993 (1991).

[34] O. A. Vydrov and T. Van Voorhis, J. Chem. Phys. **133**, 244103 (2010).

[35] H. J. Monkhorst and J. D. Pack, Phys. Rev. B **13**, 5188 (1976).

[36] W. Tang, E. Sanville, and G. Henkelman, J. Phys.: Condens. Matter **21**, 084204 (2009).

[37] W. H. Zachariasen, Phys. Rev. **40**, 917 (1932).

[38] A. Okazaki, J. Phys. Soc. Jpn. **13**, 1151 (1958).

[39] I. Gregora and W. Stetter, Phys. Status Solidi B **71**, K187 (1975).

[40] J. D. Wiley, W. J. Buckel, and R. L. Schmidt, Phys. Rev. B **13**, 2489 (1976).

[41] D. Siapkas, D. Kyriakos, and N. Economou, Solid State Commun. **19**, 765 (1976).

[42] R. Loudon, Proc. R. Soc. London, Ser. A **275**, 218 (1963).

[43] H. Chandrasekhar and U. Zwick, Solid State Commun. **18**, 1509 (1976).

[44] T. Fukunaga, S. Sugai, T. Kinosada, and K. Murase, Solid State Commun. **38**, 1049 (1981).

[45] See Supplemental Material at http://link.aps.org/supplemental/10.1103/PhysRevB.100.094301 for additional numerical calculations and plots.

[46] X. Wang, N. Mao, W. Luo, H. Kitadai, and X. Ling, J. Phys. Chem. Lett. **9**, 2830 (2018).

[47] Y. Guo, W. Zhang, H. Wu, J. Han, Y. Zhang, S. Lin, C. Liu, K. Xu, J. Qiao, W. Ji, Q. Chen, S. Gao, W. Zhang, X. Zhang, and Y. Chai, Sci. Adv. **4**, eaau6252 (2018).